Bulk rheology of sticky DNA-functionalized emulsions

Iliya D. Stoev* and Alessio Caciagli
Cavendish Laboratory, University of Cambridge, Cambridge CB3 0HE, United Kingdom

Anasua Mukhopadhyay
Department of Chemistry, Indian Institute of Technology Bombay, Mumbai 400076, India

Christopher Ness
School of Engineering, University of Edinburgh, Edinburgh EH9 3FB, United Kingdom

Erika Eiser†
PoreLab, Department of Physics, Norwegian University of Science and Technology, N-7491 Trondheim, Norway and Cavendish Laboratory, University of Cambridge, Cambridge CB3 0HE, United Kingdom

(Received 7 May 2020; revised 11 August 2021; accepted 26 September 2021; published 3 November 2021)

We measure by experiment and particle-based simulation the rheology of concentrated, non-Brownian droplet emulsions functionalized with surface-bound single-stranded (ss), "sticky," DNA. In the absence of ssDNA, the emulsion viscosity increases with the dispersed phase volume fraction ϕ, before passing through a liquid-solid transition at a critical ϕ_c related to random close packing. Introducing ssDNA leads to a liquid-solid transition at $\phi < \phi_c$, the onset being set by the droplet valency N and the ssDNA concentration (or simulated binding strength ϵ). Using insight from simulation, we identify three key behaviors: (i) jammed suspensions ($\phi > \phi_c \approx 0.64$) show weak effects of functionalization, with elastic rheology instead governed by droplet stiffness; (ii) suspensions with $\phi < \phi_c$ and $N = 1, 2$ always exhibit viscous rheology, regardless of functionalization; and (iii) for $\phi < \phi_c$ and $N > 3$, functionalization leads to a controllable viscous-elastic transition. We present state diagrams showing the range of rheological tuning attainable by these means.

DOI: 10.1103/PhysRevE.104.054602

I. INTRODUCTION

Self-assembly is a promising route for turning collections of functional objects into microstructured materials with controllable bulk mechanical properties [1–6]. DNA binding has long provided a means of directing self-assembly, initially of the molecule itself into nanoscale structures with defined architecture [7] and later through grafting to larger colloidal particles [8,9]. The specificity of base-pair attraction allows sophisticated self-assembled structures, while offering other desirable features, such as thermal reversibility and potential biocompatibility [5,6,10]. Much work focusses on submicron building blocks with surface-tethered attractive sites that assemble into prescribed structures by minimizing their free energy [11–13]. More recently, liquid droplets with surface-bound single-stranded DNA (ssDNA) have emerged as model systems for exploring hierarchical assembly of larger building blocks, often at micron scale [4,14–16]. Although microscopic architecture has been investigated in detail, the emerging bulk rheology in functionalized systems, especially in cases where the physics of jamming, glass formation, and gelation play a role, remains little explored (but see Refs. [5,6]).

Emulsions (dispersions of droplets of one liquid in another immiscible liquid) present an important model system for addressing this challenge [16–18]: Functionalized molecules can diffuse over droplet surfaces and be recruited into patches resulting in a well-defined valency [16,19,20]; they can be used to study soft particle packings spanning the jamming volume fraction ϕ_c [21,22]; and they can be synthesized with controllable droplet size [15]. Crucially, the latter makes possible "self-assembling" systems of particles large enough to render thermal diffusion negligible. Such non-Brownian systems might be useful models for food products and biological systems: Both have large constituent particles, mobile surfactants, are at or near ϕ_c, and, crucially, their rheology is an essential part of their function.

In contrast to typical (thermodynamically) self-assembling systems [23], assembly of non-Brownian components cannot proceed under ambient conditions but must be effected by external driving, for instance by shear flow. An intimate link unique to non-Brownian systems thus emerges between flow history, assembly, and the resulting rheology. The rheology of non-Brownian dispersions, in which thermal motion plays no role, is distinct from that of other colloids: Below ϕ_c the stress Σ is linear in the shear rate $\dot{\gamma}$ i.e., $\Sigma = \eta(\phi)\dot{\gamma}$; above ϕ_c the stress is rate independent, i.e., $\Sigma = k(\phi)$ [21,24–26].

*stoev@mpi-cbg.de
†ee247@cam.ac.uk

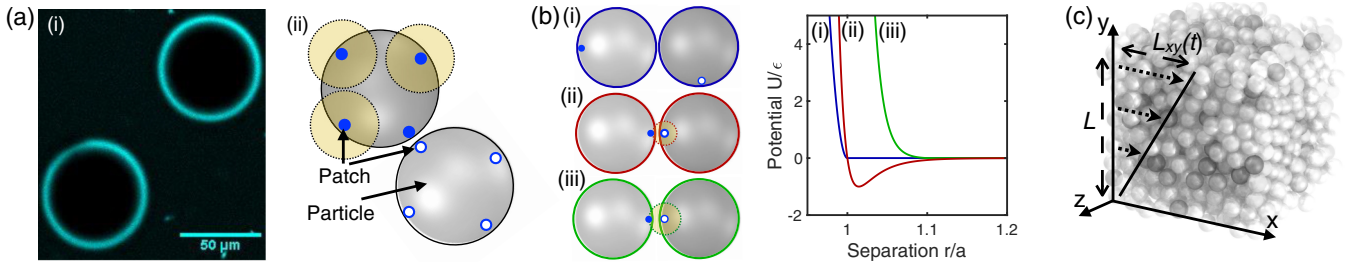

FIG. 1. Non-Brownian droplets functionalized with ssDNA. (a) (i) Confocal image of the experimental system showing functionalized droplet surfaces; (ii) simulation model showing four pairs of complementary patches on two droplets. (b) Sketches of droplet pairs and their associated droplet-droplet interaction potential, approaching with patches (i) misaligned; (ii) complementary; and (iii) noncomplementary. (c) An assembly of droplets with dotted arrows indicating the velocity gradient imposed during shearing.

The current state of such a suspension therefore depends on the strain history applied to it, though not the rate at which previous strains were applied. Meanwhile, above ϕ_c the stiffness of the particles matters and the suspension exhibits elastic rheology [27]. Thus, a viscous-to-elastic transition occurs as ϕ is increased. Self-assembly presents an opportunity to manipulate this rheology by enhancing the viscous and elastic regimes or, indeed, by effecting a viscous-to-elastic transition away from ϕ_c. Doing so would make possible the use of such materials in applications in which both microstructure and bulk rheology are key to function.

Realizing the potential of driven assembly of functionalized non-Brownian particles for controlled rheology requires first understanding the physics that enter under the addition of functionalized sites of basic complementarity. Here we address this using experiments and simulations, demonstrating the effect of mixing complementary A and A' functionalized droplets on the rheology of a non-Brownian emulsion. Below ϕ_c, there is a dramatic effect whereby a viscous emulsion transitions to being elastic as ssDNA is added. The effect above ϕ_c is more modest but reveals the rheological fine-tuning that may be achieved by careful functionalization. We further use the simulation to provide insight into structure formation under various conditions. Our results demonstrate that driven assembly enables rheological tuning, establishing a new model system in which to address the macroscopic physics of functionalized non-Brownian particles.

II. EXPERIMENTAL METHOD

Silicone oil-in-water emulsions with azide-functionalized Synperonic F108 (Sigma Aldrich) surfactant are generated by membrane emulsification. For nonfunctionalized emulsions, desired oil droplet volume fractions ϕ are obtained using an evaporation method consisting of extraction of homogenized emulsions followed by incubation at 65 °C. Subsequent up-concentration is achieved by removal of the subnatant following creaming. From microscopy, the mean droplet diameter is 35.6 ± 7.1 μm (polydispersity index 0.20). For functionalized emulsions, we start with two partially complementary amino-ssDNA sequences (Integrated DNA Technologies) consisting of 15T-long spacers and a nine-base-long sticky overhang and use a copper-free click-chemistry reaction to replace the amino groups with dibenzylcyclooctane (DBCO) functional groups [15]. We then prepare functionalized droplets by mixing up to 40 nmol of the resulting DBCO-DNA per 100 μl of bare emulsion (at $\phi \approx 0.76$). [Mixing DBCO stained with cyanine-5 dye (DBCO-Cy5, Sigma-Aldrich) confirms the attachment of DBCO-functionalized molecules to the azide-F108 surfactant-stabilized droplets, Fig. 1(a(i))]. A-ssDNA and A'-ssDNA functionalized droplets are incubated separately for 24 h at 65 °C, after which they are mixed in equal volumes and then brought to the ϕ of interest (to within 2–3%) by removing the subnatant following creaming. Temperature cycling between 20° and 60 °C demonstrates reversibility (albeit limited by the diffusion rate of the large droplets) of binding, verifying that the droplets are indeed bound through DNA. Steady and oscillatory rheology measurements are taken at 20 °C using a stress-controlled rheometer (MCR 501, Anton-Paar, Physica) equipped with a cone-and-plate geometry (25-mm diameter base and 2° cone angle), preventing evaporation using a custom-made vapour trap. Further details are given in Refs. [15,28].

III. NUMERICAL METHOD

We simulate the trajectories of neutrally buoyant, polydisperse (radii uniformly distributed in the range 0.9a–a, to inhibit crystallization) spherical droplets subject to short-ranged hydrodynamic and repulsive contact forces. The droplets have fixed numbers of "patches," attractive sites that move freely over their surfaces [Fig. 1(b)] and experience shear with flow direction in x and gradient in y [Fig. 1(c)]. By setting the number N, attractive strength and complementarity of the patches, we prescribe binding rules that lead to specific microstructures and govern the rheology of the material. The periodic simulation box contains $\mathcal{O}(10^3)$ droplets of density ρ at volume fraction ϕ.

A. Interaction forces

Hydrodynamic forces $\boldsymbol{F}^h$ and torques are calculated identically to Ref. [29] (see also Ref. [22]), taking into account Stokes drag and regularized pairwise lubrication. We omit long-range hydrodynamics, assuming them to be screened at the large ϕ of interest here. Overlapping droplets are subject to repulsive forces $\boldsymbol{F}^c$. For a contacting droplet pair with overlap $\delta = (a_1 + a_2) - |\boldsymbol{r}|$ for radii a_i and center-center vector $\boldsymbol{r}$, the force (with stiffness k) is $\boldsymbol{F}^c = k\delta\boldsymbol{r}/|\boldsymbol{r}|$.

Attractive patches are modelled by locating N smaller particles on host droplet surfaces. Patches are connected to hosts via stiff springs with a harmonic potential, leading to a force with magnitude $F^b = k_s(0.8a - r)$, where r is the patch-host center-center distance and k_s is sufficiently large so that patches are essentially fixed at 0.8a from their host droplet center, though they are free to move over the host surface at no cost (patch motion is typically considered to be fast compared to droplet motion and rotation [4,16]). Patches interact through forces $\boldsymbol{F}^p$ set by a Mie potential [30], chosen for its simple form with tuneable attractive or repulsive strength and range:

$$U(r) = C\epsilon\left\{\left(\frac{\sigma}{r}\right)^{\gamma_\alpha} - \left(\frac{\sigma}{r}\right)^{\gamma_\beta} - \left[\left(\frac{\sigma}{r_c}\right)^{\gamma_\alpha} - \left(\frac{\sigma}{r_c}\right)^{\gamma_\beta}\right]\right\}, \quad (1)$$

with $C = f(\gamma_\alpha, \gamma_\beta)$ [31] ($\gamma_\alpha = 20$ and $\gamma_\beta = 10$), r the patch-patch distance, and $\sigma = 0.2a$ the zero-crossing distance. We specify the strength of interactions using ϵ and the specificity by cutting off the potential at r_c. For complementary patches, we set $r_c = 2\sigma$. For noncomplementary patches, we set $\sigma = 0.35a$ and $r_c = \sigma$, suppressing the attractive part of the potential. The larger value of σ in the latter case introduces steric hindrance inhibiting multiple bonds between patches. Simulations contain equal numbers of A and A' droplets, represented by the shaded and unshaded patched droplets in Fig. 1(a(ii)). In order to attract, patches must be of the same color but opposite shadedness. The overall droplet-droplet interactions are sketched in Figs. 1(b).

B. Control parameters

The above forces are summed on each droplet and used to calculate trajectories, and the stress tensor $\boldsymbol{\Sigma}$ is computed by summing $(\boldsymbol{F} \times \boldsymbol{r})$ over all interacting pairs and averaging over at least five realizations. The model naturally permits droplet inertia, which may become relevant when $\hat{\dot{\gamma}}$ (see below) and ϕ are large. Three key control parameters emerge in addition to the volume fraction ϕ and valency N: (i) Stokes number $\rho\dot{\gamma}a^2/\eta_f$ for suspending fluid viscosity η_f and shear rate (defined below) $\dot{\gamma}$, set $\ll 1$ throughout to approximate overdamped conditions; (ii) droplet stiffness, nondimensionalized as $\hat{\dot{\gamma}} = 2\dot{\gamma}a/\sqrt{k/(2\rho a)}$ [32,33], set $< 10^{-2}$ throughout to approximate hard spheres (noting that decreasing this quantity leads to a soft particle regime [25]); and (iii) patch attraction strength or "stickiness," written as $\hat{\epsilon} = \epsilon/\eta_f\dot{\gamma}a^3$. The latter quantity compares the stress associated with attractions (ϵ/a^3) with the viscous stress. Setting $\hat{\epsilon} \gtrsim 1$ leads to irreversibly strong complementary patch attraction, mimicking the experimental conditions at 20 °C. The model is implemented in LAMMPS [31] (see also Ref. [34]).

C. Obtaining rheological quantities

We measure the shear stress Σ while deforming the box according to either $\gamma(t) = \dot{\gamma}t$ or $\gamma(t) = \gamma_0 \sin(\omega t)$. In the former we define the viscosity as $\eta = \Sigma/\dot{\gamma}$; in the latter we measure G' and G'' from the response $\Sigma(t) = \Sigma_0 \sin(\omega t + \delta)$, taking a linear approximation [35,36] (this is accurate up to around $\gamma_0 \sim 10^{-1}$; at larger γ_0, it is satisfactory for our current purposes, though is the subject of further analysis in the literature [35–37]). Oscillatory shear is applied with flow in x and velocity gradient in y so that the strain follows $\gamma(t) = L_{xy}(t)/L = \gamma_0 \sin(\omega t)$ [see Fig. 1(c)] and $\dot{\gamma}(t) = \omega\gamma_0 \cos(\omega t)$. We remain in the low-frequency regime throughout, so elastic responses are independent of the strain rate [cf. (ii) above], whereas viscous responses scale linearly with the strain rate [cf. (i) above]. The moduli, given by $G' = \frac{\Sigma_0}{\gamma_0}\cos\delta$ and $G'' = \frac{\Sigma_0}{\gamma_0}\sin\delta$, quantify, respectively, the elastic and viscous responses. We nondimensionalize the moduli measured by simulation with a/k, the viscosity using the continuous phase value as η/η_f, and ϵ has units $\eta_f^2 a/\rho$.

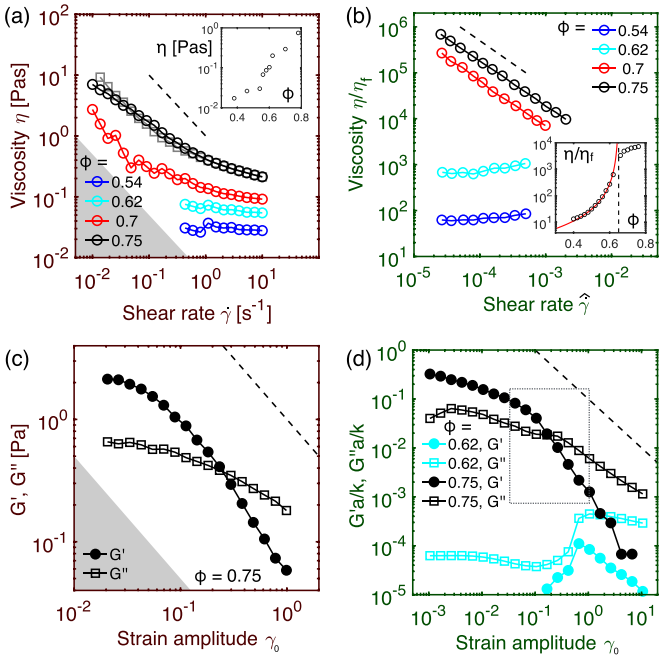

FIG. 2. Rheology of bare emulsions. Steady shear rheology $\eta(\dot{\gamma}, \phi)$ measured (a) experimentally and (b) by simulation. Dashed lines indicate $\eta \propto \dot{\gamma}^{-1}$. Gray points in (a) show the viscosity measured by backward ramp. Inset of (a) shows experimental $\eta(\phi)$ at $\dot{\gamma} = 10\,\mathrm{s}^{-1}$; inset of (b) shows $\eta/\eta_f(\phi)$ at $\hat{\dot{\gamma}} \sim 0.001$, with the red line a fit to $\eta \propto (1 - \phi/\phi_c)^{-2}$ and the dashed line indicating ϕ_c. Strain amplitude sweeps $G'(\gamma)$, $G''(\gamma)$ measured by (c) experiment and (d) simulation. Dashed lines indicate G', $G'' \propto \gamma^{-1}$. Gray box in (d) indicates the range of γ_0 measured in (c). For experimental data, the marker size represents approximate errors and gray panels show region of experimental inaccessibility.

IV. RESULTS

A. Rheology of bare droplets

We first discuss steady shear viscosity measurements $\eta(\phi, \dot{\gamma})$ obtained by experiment and simulation in the absence of functionalization, Figs. 2(a) and 2(b). For $\phi = (0.54, 0.62)$, both predict quasi-Newtonian rheology. Here η increases sharply with ϕ and the rate dependence is rather weak due to the absence of thermal motion [24]. The tolerance of the rheometer sets a limit on the minimum shear rate accessible for these ϕ [gray region in Fig. 2(a)]. For $\phi = (0.7, 0.75)$ there is clear shear-thinning approaching a -1 power law [$\eta \propto \dot{\gamma}^{-1}$ so that $\Sigma \neq f(\dot{\gamma})$] [dashed lines in Figs. 2(a) and 2(b)], indicative of elastic yield-stress behavior [21,26]. Our

experimental yield stress of ≈0.1 Pa is consistent with [38] after taking into account the disparity in a. A forward-and-reverse shear-rate ramp at $\phi = 0.75$ [Fig. 2(a)] demonstrates only minor hysteresis, suggesting minimal evaporation, droplet coalescence or rupturing across the range of $\dot{\gamma}$ and Σ explored.

The viscosity predicted by simulation at low ϕ is modelled as $\eta/\eta_f \propto (1-\phi/\phi_c)^{-2}$ [39] [Fig. 2(b) (inset)], leading to $\phi_c \approx 0.64$ [precise experimental determination of ϕ_c is difficult as the transition becomes rather smooth at large $\dot{\gamma}$, Fig. 2(a) (inset)]. $\phi_c \approx 0.64$ is reminiscent of the random close packing value found for frictionless monodisperse spheres. Above ϕ_c, droplet-droplet interactions dominate, and the viscosity increases more slowly with ϕ, taking on a 2/3 power law [33] with magnitude that depends on the droplet stiffness [25].

We next characterize the rheology of bare droplets under oscillatory shear using strain ramps, Figs. 2(c) and 2(d), with the experimental frequency ω set sufficiently low that there is minimal ω dependence in the presented results. For $\phi > \phi_c$ and small γ_0, both experiments and simulations give $G' > G''$, indicating elastic rheology consistent with the shear-thinning behavior found above. The crossover strain (the value of γ_0 at which $G' = G''$) is in agreement with literature data [38,40]; larger strains lead to a nonlinear rheological response, in which our linear approximation for evaluating G', G'' breaks down.

For $\phi < \phi_c$ and small γ_0, the simulation predicts $G'' \gg G'$, indicating a viscous response, Fig. 2(d). This matches our numerical and experimental finding for steady shear and is consistent with experimental measurements of the moduli in a concentrated suspension of solid particles with a more viscous continuous phase [37]. Our experimental sample does not permit measurement of the moduli for $\phi < \phi_c$ as the low solvent viscosity renders the stress close to the tolerance of the device. Together, the shear and oscillatory results demonstrate concisely that our system is a good model for non-Brownian emulsion rheology. It exhibits viscous and elastic rheology at low and high ϕ respectively (separated by a jamming transition), consistent with literature data [41–43] and forming a baseline on which to interpret the rheology of functionalized emulsions in what follows.

B. Rheology of functionalized oil droplets

We next turn to functionalized emulsions, in which droplet-droplet attraction is introduced experimentally and computationally ($N = 6$) as described above. We show first the dramatic effect of functionalizing emulsions below jamming, $\phi < \phi_c$, Figs. 3(a) and 3(b). For the same reasons as described above, we use continuous (as opposed to oscillatory) shear to probe experimentally the low-ϕ behavior. We find, Fig. 3(a), that on slowly increasing the amount of ssDNA added from 1 nmol to 20 nmol per 100 μl of stock $\phi = 0.76$ (which are subsequently diluted) droplets, the emulsion viscosity first increases while retaining its roughly quasi-Newtonian form. As we increase the added ssDNA to 40 nmol, though, we find a dramatic jump to shear-thinning rheology, reminiscent of the jammed behavior observed in Fig. 2(a) on increasing ϕ, albeit of a different nature. Points

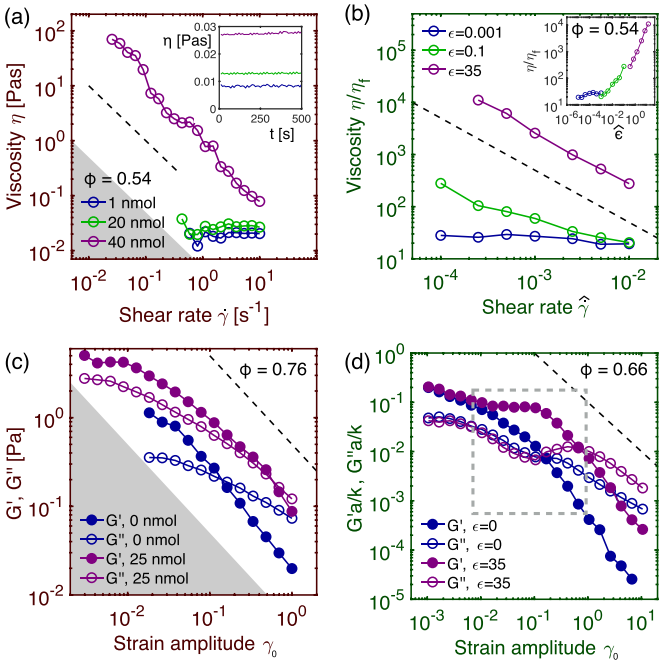

FIG. 3. Rheology of functionalized emulsions. (a) Experimental measurements under continuous shear for $\phi = 0.54 < \phi_c$. Shown are different amounts of ssDNA added per 100 μl of stock droplets: 1 nmol (blue), 20 nmol (green), and 40 nmol (purple); inset of (a) shows $\eta(t)$ at $\dot{\gamma} = 10\ \mathrm{s}^{-1}$ for different amounts of ssDNA at $\phi \approx 0.54$; (b) simulation predictions corresponding to (a), where we vary the attraction ϵ. Shown in the inset are the same data plotted against $\hat{\epsilon}$; (c) experimental measurements under oscillatory shear for $\phi = 0.76 > \phi_c$. Shown is a comparison between bare (blue) and functionalized (25 nmol DNA added per 100 μl of droplets, purple) jammed emulsions; (d) Simulation predictions corresponding to (c), with two different ϵ. Filled (empty) symbols represent G' (G''). The dashed box in (d) indicates the experimentally probed region. Gray panels show regions of experimental inaccessibility.

in Fig. 3(a) represent time averages; there is a modest upward drift with time due to sample evaporation, Fig. 3(a) (inset). Our simulation result for $\phi = 0.54$, Fig. 3(b), closely parallels this, showing, in the (near) absence of functionalization ($\epsilon = 0.001$), a viscous response for all $\dot{\gamma}$, and a shear-thinning response at larger ϵ. In both experiment and simulation, the viscous rheological response (i.e., linear dependence of Σ on $\dot{\gamma}$) thus transitions to an elastic response on increasing attraction. At low ϕ the ssDNA concentration can thus be used as a "switch" to set the rheology of the non-Brownian emulsion.

Above jamming, $\phi > \phi_c$, the effect of adding functionalization is rather more subtle. Both experiment and simulation predict that the emulsion is already in a jammed state, with G' dominating the rheology [cf. Figs. 2(c) and 2(d)]. As such, adding functionalization is expected to have a less dramatic effect when compared with the low-ϕ result. Nonetheless, there are important consequences, as shown in Figs. 3(c) and 3(d). First, adding functionalization leads to a modest increase in the moduli for small γ_0. In the jammed state, the dominant contribution to the stress comes from droplet squeezing. However, adding functionalization means that to

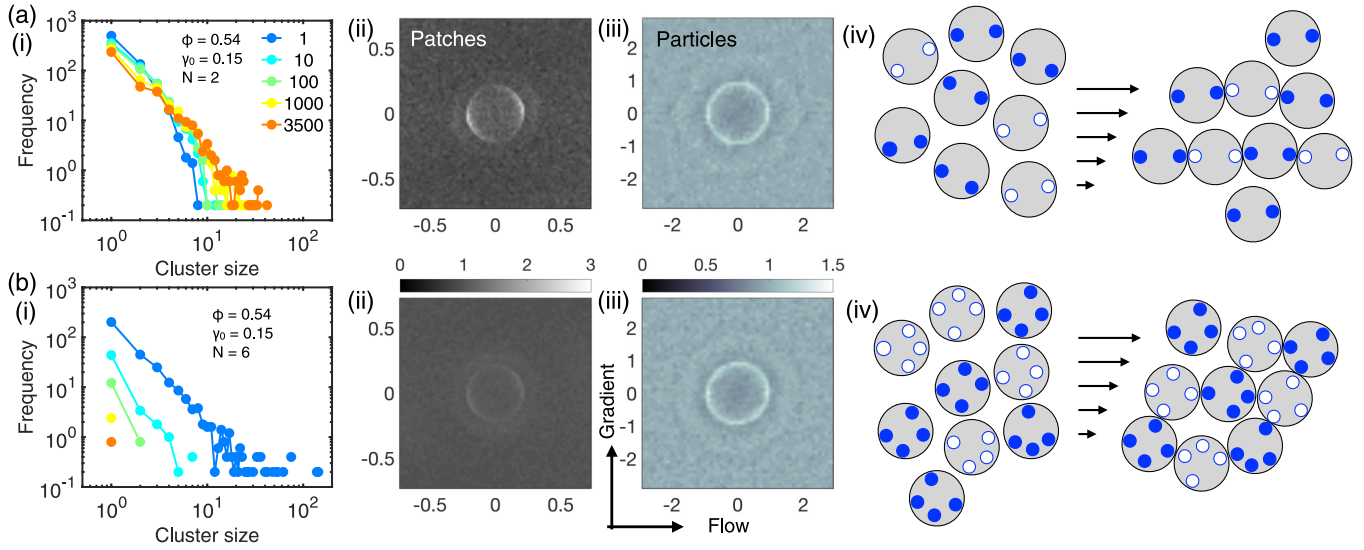

FIG. 4. Shear-induced assembly of droplet chains and clusters in a suspension at $\phi = 0.54$ sheared with $\gamma_0 = 1$ for $\mathcal{O}(10)$ oscillatory cycles. Shown for (a) valency $N = 2$ and (b) $N = 6$ are (i) the distribution of cluster sizes across a range of $\hat{\epsilon}$ as shown in the legend; two-dimensional representations of the radial distribution function showing patches (ii) and droplets (iii) with $\hat{\epsilon} = 3500$ aligning along the flow direction; (iv) sketches of assembled chains and clusters (showing in the bottom row only four patches for clarity, though there are 6 in the simulation). Black arrows indicate direction of shearing and velocity gradient. Droplets with valency $N = 2$ form chains, the bonds of which become aligned in the flow direction, while the bulk arrangement of the droplets remains rather isotropic. Droplets with valency $N = 6$ form percolating networks for large $\hat{\epsilon}$ and retain a largely isotropic structure.

achieve even small deformations, we must stretch some of the tethered droplet-droplet bonds, requiring an additional stress.

Second, adding functionalization leads to a shift to the right of the crossover strain γ_c. This represents the onset of plastic deformations, where droplets start to rearrange with respect to one another [44]. These plastic, irreversible steps lead to energy dissipation, resulting in an increase of G'' relative to G'. Attractive interactions between droplets make it harder to achieve such displacements. Therefore, we need to go to higher strains and, consequently, higher stresses, in order to reach the yielded state. It is important to note here that yielding does not necessarily require the breakage of droplet-droplet bonds. Since the functionalized sites are mobile on the droplet surfaces, considerable reorientation is allowed without breaking them, making difficult a characterization of the mechanisms at play. Again, the simulation at $\phi > \phi_c$, Fig. 3(d), closely predicts the important rheological changes effected by the functionalization. Having established the success of the simulation in capturing experimental bulk rheology, we next focus on the role of droplet valency in the simulation, addressing structure formation and rheology.

C. Role of droplet valency in simulated system

1. Structure formation

We take as examples cases with $\phi = 0.54$ and valencies $N = 2$ and $N = 6$ and reiterate that, in our non-Brownian system, droplets do not move under quiescent conditions but must be induced to do so by external driving. This is achieved here by applying oscillatory shear as described above, with the resultant structures being products of the flow history.

Samples are prepared by first applying shear at $\gamma_0 = 0.15$ for $\mathcal{O}(10)$ cycles with $\hat{\epsilon} = [1, 10, 100, 1000, 3500]$. This amplitude is large enough to bring droplets into contact with immediate neighbors but small enough that there is no large-scale rearrangement of the structure. Shown in Fig. 4 are, for $N = 2$ [Fig. 4(a)] and $N = 6$ [Fig. 4(b)], the resulting cluster size distributions (i), radial distribution functions for patches (ii) and droplets (iii) projected onto the flow-gradient plane, and sketches illustrating the assembly and alignment of droplets occurring during flow (iv). Clusters are defined unambiguously as sets of droplets connected by patch-patch bonds.

For $N = 2$, complementarity dictates that droplets assemble into chains. The data show a power-law distribution of cluster sizes (i.e., chain lengths), with the average size increasing steadily with $\hat{\epsilon}$. This suggests that for small $\hat{\epsilon}$, competition between viscous forces and patch attraction is sufficient to prevent all complementary patches from binding. For large $\hat{\epsilon}$ all complementary patches that come within range will successfully form bonds. The maximum chain length reaches up to 40 droplets, indicating that chains loop over periodic boundaries. Even for large $\hat{\epsilon}$, there remain many unbound droplets, as expected due to the limited exploration of the phase space achievable under $\gamma_0 = 0.15$. The radial distribution functions in Figs. 4(a(ii)) and 4(a(iii)) reveal a hierarchical structure in which the patches align along the flow direction, whereas the overall arrangement of the droplets remains largely isotropic [Fig. 4(a(iv))]. The repeated switching of compressive and extensional directions under oscillatory shear thus leads to chains positioned parallel to the flow direction.

Meanwhile, for $N = 6$, the cluster size distribution indicates a percolation transition taking place as $\hat{\epsilon}$ is increased, with formation of system-spanning clusters, leaving $\mathcal{O}(1)$ unbound droplets. Despite the relatively small γ_0, droplets

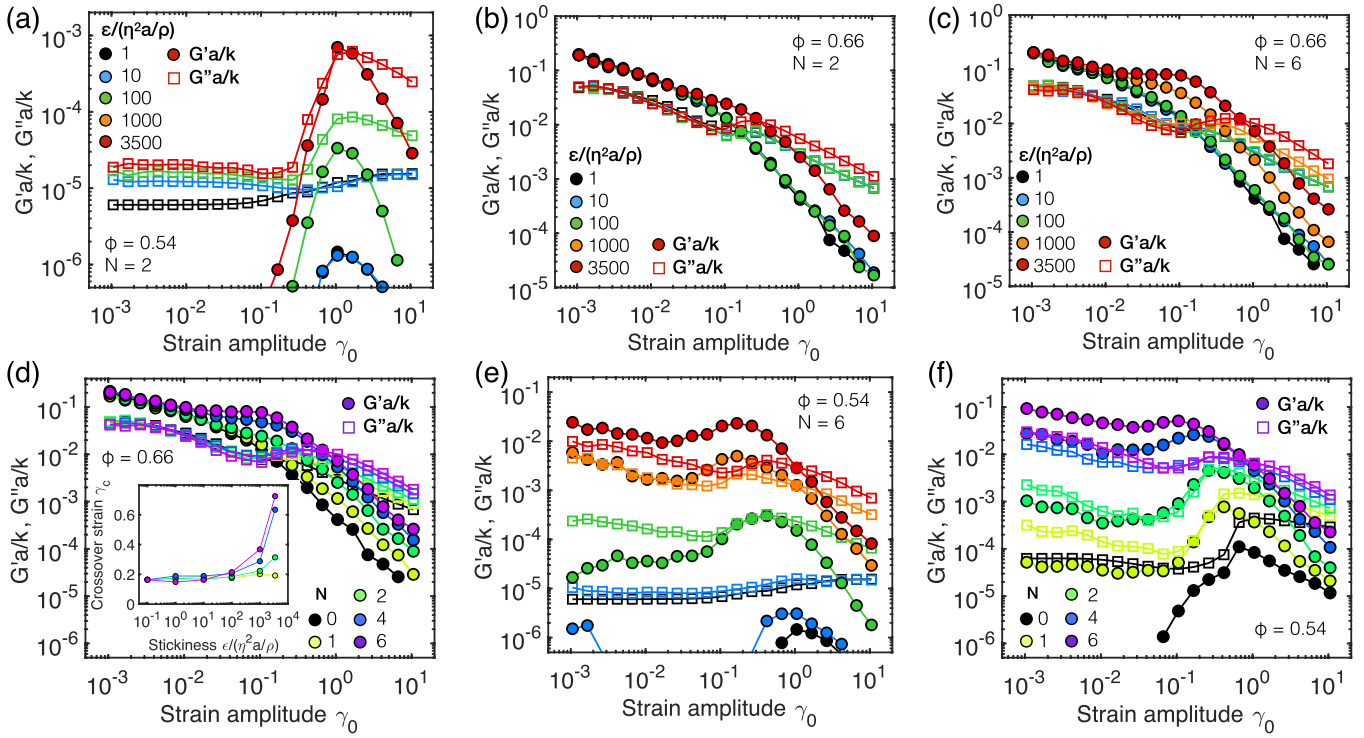

FIG. 5. Strain amplitude γ_0 sweeps for various volume fractions ϕ, valencies N, and attractive strengths $\hat{\epsilon}$. Shown in (a)–(c) and (e) are the storage G' and loss G'' moduli at different $\hat{\epsilon}$ [given in legend of (a)–(c)] for (a) $\phi = 0.54$, $N = 2$; (b) $\phi = 0.66$, $N = 2$; (c) $\phi = 0.66$, $N = 6$; and (e) $\phi = 0.54$, $N = 6$. The moduli are scaled by the droplet radius and stiffness as $G'a/k$ and $G''a/k$. Shown in (d) and (f) are G' and G'' for valencies $N = [0, 1, 2, 4, 6]$ at $\phi = 0.66$ (d) and $\phi = 0.54$ (f). The inset of (d) shows the crossover strain γ_c as a function of $\hat{\epsilon}$ for $\phi = 0.66$. Throughout, solid circles represent storage moduli G', while hollow squares represent loss moduli G''.

form sufficient patch-patch bonds to assemble into such clusters. Importantly, it is not necessary to achieve six bonds per droplet (commensurate with $N = 6$) to reach percolation: This can be achieved with as few as three bonds per droplet. With $N = 6$, the alignment of patches is more isotropic: In order to form up to six bound neighbors, avoidance of steric hindrance requires that patches be distributed more uniformly across droplet surfaces. As for $N = 2$, the droplet radial distribution function is largely isotropic [Fig. 4(b(iv))].

2. *Rheology*

We next explore the simulated rheology as a function of N, taking as our input microstructured systems presheared as described above (but with varying γ_0) We measure G' and G'' as functions of strain amplitude γ_0, volume fraction ϕ, valency N, and attractive strength $\hat{\epsilon}$, finding that the results can be categorized broadly into three regimes:

(i) Always viscous, Fig. 5(a). For $\phi < \phi_c \approx 0.64$, the material has a viscous response in the absence of attractive interactions. On increasing the attractive strength above $\hat{\epsilon} = 10$ with $N = 2$, we find for low γ_0 an increase in G'' as droplets are bound together by patches to form chains. These larger structures lead to enhanced dissipation, resulting in larger stresses and a more viscous response. There is a surge in the response at $\gamma_0 \approx 0.2$, marking the onset of plastic rearrangements and diffusion as droplets must flow over one another to conform to the shearing flow. This leads to a nonlinearity in the stress that gives rise to an appreciable G', which eventually subsides for yet larger γ_0. This γ_0-dependent stress response is similar to that reported previously in sheared granular suspensions [37]. This "always viscous" response is predicated on the valency being sufficiently low to avoid percolation of the bound network.

(ii) Always elastic, Figs. 5(b)–5(d). For $\phi = 0.66 (> \phi_c)$, the low-γ_0 response is elastic for all $\hat{\epsilon}$ and N, and indeed there is no substantial rheological difference observed when varying these quantities. Here the rheology is dominated by the elasticity of the droplets themselves: The moduli scale directly with k [45], while the volume fraction dependence is given by $|\phi - \phi_c|^{2/3}$ [33].

Nonetheless the patches have an important effect on the bulk rheology as γ_0 is increased. Specifically, the position of the G'-G'' crossover [which occurs at γ_c, see Fig. 5(d) (inset)] and the large-γ_0 behavior depend weakly on N and $\hat{\epsilon}$. As we increase γ_0 above $\gamma_c = \mathcal{O}(0.1)$, we explore the stretching of bonds between complementary droplets, evidenced by a surge in G'. Thus, $\hat{\epsilon}$ dependence enters. As interdroplet bonds get stronger, the material remains elastic at progressively larger strain amplitudes, manifested as an increase in γ_c; that is, increasing the valency delays yielding of the material. This effect is borne out particularly for $N = 4, 6$ [Fig. 5(d) (inset)]. Beyond γ_c, we find an increase in both G' and G'' as both N and $\hat{\epsilon}$ are increased. The latter effect is more pronounced for large N [comparing Figs. 5(b) and 5(c)], since stretching and breaking larger numbers of patch-patch bonds will require larger stresses.

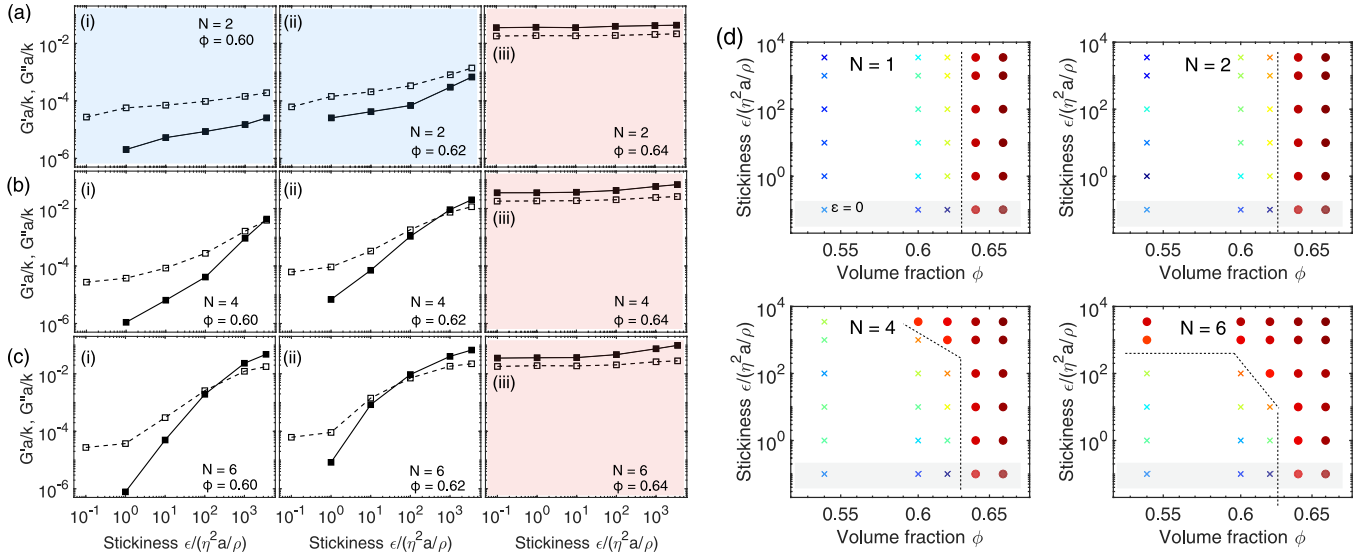

FIG. 6. Rheological response at low strain amplitude, $\gamma_0 = 10^{-3}$. Shown in (a)–(c) are the storage G' and loss G'' moduli measured at the steady state for (a) $N = 2$, (b) $N = 4$, and (c) $N = 6$, with volume fractions (i) $\phi = 0.60$, (ii) $\phi = 0.62$, and (iii) $\phi = 0.66$. Throughout, the moduli are scaled by the droplet radius a and stiffness k. Highlighted in blue and red are, respectively, the viscous and elastic regimes, while the crossover regime is in white. (d) Flow state diagrams, comprising all of the simulated emulsions in this work, measured with $\gamma_0 = 10^{-3}$. Crosses indicate $G'' > G'$; filled circles represent $G' > G''$. The color scale represents the magnitude of the stress response (i.e., $\Sigma_0 a/k$), increasing in value from light blue to dark red. Dashed lines represent the approximate boundaries that mark viscous-elastic transitions. Shown in the grayed regions are results for nonfunctionalized droplets $\hat{\epsilon} = 0$. Data are given for valencies $N = (1, 2, 4, 6)$.

(iii) Crossover region, Figs. 5(e) and 5(f). For low volume fraction $\phi < \phi_c$ and high valency $N > 2$ (so that a percolating network can form), elastic behavior emerges at low γ_0 as a function of $\hat{\epsilon}$. Shown in Fig. 5(e) are data with $N = 6$, $\phi = 0.54$ and increasing $\hat{\epsilon}$. The crossover occurs in this case for $\hat{\epsilon} \approx 1000$, above which $G' > G''$ at small γ_0. Meanwhile, in Fig. 5(f) are data for $\hat{\epsilon} = 3500$, $\phi = 0.54$ and increasing N. With $N = 4$, 6, the results are clearly elastic for small γ_0, whereas for smaller N, they are viscous. These values of N are significant. In order to exhibit an elastic response, the suspension must have a percolating, networklike microstructure, possible only when branching can occur.

D. Regime maps

The low-γ_0 crossover behavior of these three regimes is summarized in Figs. 6(a)–6(c). These data effectively present a road map of the rheological behavior obtainable in our simulated model emulsion. Shown in the highlighted light blue frames are those results (low valency N and $\phi < \phi_c$) for which the response is always viscous. Here the volume fraction ϕ is sufficiently low that in the absence of functionalization the stresses under shear simply scale with the rate $\dot{\gamma}$. With $N = 2$ patches, the droplets can form chainlike structures, but in the absence of a percolating network, the response remains viscous, albeit with an enhanced viscosity. Shown in the highlighted light red frames are those results ($\phi > \phi_c$ and all N, $\hat{\epsilon}$) for which the response is always elastic. Here the rheology is dominated by droplet-droplet repulsive forces and the presence of functionalization is only relevant at large γ_0, and even there the influence of patches is rather weak. Finally, in white are those results ($\phi < \phi_c$ and high valency $N > 2$) for which the response can be tuned between viscous and elastic by adjusting $\hat{\epsilon}$. Here the strength of patch-patch attraction can dictate whether or not percolating networks form and thus whether the rheology is elastic.

We finally present in Fig. 6(d) regime maps, summarizing the range of rheological behaviors obtained as functions of volume fraction ϕ and stickiness $\hat{\epsilon}$ for valencies $N = 1$, 2, 4 and 6, and with $\gamma_0 = 10^{-3}$. A few pertinent results emerge: (i) Regardless of attraction strength $\hat{\epsilon}$, we can never force an elastic response $G' > G''$ in a system below ϕ_c with valency $N = 1$ or 2. This follows naturally from a constraint-counting argument. With $N = 2$, we essentially have a system of frictionless spheres connected into freely jointed chains. Such spheres require an average of six contacts to reach isostaticity: The bonds due to functionalization provide two (even in the limit $\hat{\epsilon} \to \infty$); achieving another four requires $\phi > \phi_c$; (ii) Jammed suspensions ($\phi > \phi_c$) show rather weak effects of functionalization. The simulation data suggest that this is because the stresses are already dominated by elasticity of the droplets. As γ_0 is increased, the functionalization begins to play a role, leading to a shift to the right of the G'-G'' crossover strain γ_c, from $\gamma_c = 0.2$ to $\gamma_c \approx 6$. (iii) Only for $N > 3$ and $\phi < \phi_c$ does the regime (solid or liquid) depend on both N and $\hat{\epsilon}$.

V. CONCLUDING REMARKS

We have presented experimental and numerical rheology results for a functionalized non-Brownian emulsion, with attraction controlled experimentally using ssDNA concentration and numerically with selectively attractive patches. The outcomes provide a set of principles on which tunable rheology might be realized in model systems of more complex complementarity. Our numerical results predict that doing

so requires, crucially, fine control over the volume fraction ϕ as well as an ability to set the droplet valency [17,20]. Importantly, the fact that the generated structures have fabric commensurate with the strain rate suggests that exotic flow protocols, for instance combinations of steady shear and oscillations, might be exploited to generate more complex structures or to maximize the extent of assembly. Tuning the microstructure through this type of complex, prescribed flow history might influence the success of assembly by analogy to fluctuations or controlled tuning of the temperature or interactions in thermal systems [46,47].

Having established the basic behavior achievable with a simplistic binding complementarity, we anticipate that this work will lead to more extensive investigation into details of how the introduction of ssDNA (or indeed other selectively attractive molecules) can modify the rheology of emulsions of various sizes, levels of polydispersity and complexity of complementarity. Our simulation model substantively corroborates the experimental phenomenology, offering a complementary platform for both microstructural scrutiny and rapid exploration of parameter space.

Further work is required to demonstrate the full potential of this capability. For instance, the valency is easy to control numerically while experimental results are emerging on the formation of well-defined attractive patches [16]. By establishing the relationship between ssDNA concentration and patch formation, one can investigate the effect of valency more systematically. Meanwhile, it will be important to understand the rheological significance of using different types of oils and surfactants for forming and stabilizing the droplets, respectively. For example, differences in solubility can strongly affect droplet size distributions [15], while the F108 surfactant used here has, in contrast to other surfactants, an inverse phase diagram: an aqueous solution of the pure surfactant is liquid at low temperatures, but gels when heated. Future progress in understanding and controlling the rheology of emulsions is expected to impact formulation of products in personal care, food and other sectors.

ACKNOWLEDGMENTS

I.D.S. thanks the EPSRC (Grant No. 1805384) for funding the experiments performed in this study. A.C. and E.E. acknowledge ETN-COLLDENSE (H2020-MCSA-ITN-2014, Grant No. 642774) and the Winton Program for the Physics of Sustainability. A.M. acknowledges the Commonwealth Scholarship Commission (UK government) and the Department of Chemistry, IIT Bombay, India. C.N. acknowledges financial support from the Maudslay-Butler Research Fellowship at Pembroke College, Cambridge and latterly from the Royal Academy of Engineering under the Research Fellowship scheme.

[1] G. M. Whitesides and B. Grzybowski, Science **295**, 2418 (2002).
[2] N. C. Seeman, Annu. Rev. Biophys. Biomol. Struct. **27**, 225 (1998).
[3] C. K. McLaughlin, G. D. Hamblin, and H. F. Sleiman, Chem. Soc. Rev. **40**, 5647 (2011).
[4] Y. Zhang, X. He, R. Zhuo, R. Sha, J. Brujic, N. C. Seeman, and P. M. Chaikin, Proc. Natl. Acad. Sci. USA **115**, 9086 (2018).
[5] I. D. Stoev, T. Cao, A. Caciagli, J. Yu, C. Ness, R. Liu, R. Ghosh, T. ONeill, D. Liu, and E. Eiser, Soft Matter **16**, 990 (2020).
[6] Z. Xing, A. Caciagli, T. Cao, I. Stoev, M. Zupkauskas, T. O'Neill, T. Wenzel, R. Lamboll, D. Liu, and E. Eiser, Proc. Natl. Acad. Sci. USA **115**, 8137 (2018).
[7] N. C. Seeman, Nature (London) **421**, 427 (2003).
[8] N. Geerts and E. Eiser, Soft Matter **6**, 4647 (2010).
[9] L. Di Michele and E. Eiser, Phys. Chem. Chem. Phys. **15**, 3115 (2013).
[10] J. Fernandez-Castanon, S. Bianchi, F. Saglimbeni, R. Di Leonardo, and F. Sciortino, Soft Matter **14**, 6431 (2018).
[11] J. D. Halverson and A. V. Tkachenko, Phys. Rev. E **87**, 062310 (2013).
[12] K.-T. Wu, L. Feng, R. Sha, R. Dreyfus, A. Y. Grosberg, N. C. Seeman, and P. M. Chaikin, Phys. Rev. E **88**, 022304 (2013).
[13] A. Reinhardt and D. Frenkel, Phys. Rev. Lett. **112**, 238103 (2014).
[14] D. Joshi, D. Bargteil, A. Caciagli, J. Burelbach, Z. Xing, A. S. Nunes, D. E. Pinto, N. A. Araújo, J. Brujic, and E. Eiser, Sci. Adv. **2**, e1600881 (2016).
[15] A. Caciagli, M. Zupkauskas, A. Levin, T. P. J. Knowles, C. Mugemana, N. Bruns, T. O'Neill, W. J. Frith, and E. Eiser, Langmuir **34**, 10073 (2018).
[16] Y. Zhang, A. McMullen, L.-L. Pontani, X. He, R. Sha, N. C. Seeman, J. Brujic, and P. M. Chaikin, Nat. Commun. **8**, 21 (2017).
[17] L. Feng, L.-L. Pontani, R. Dreyfus, P. Chaikin, and J. Brujic, Soft Matter **9**, 9816 (2013).
[18] A. McMullen, M. Holmes-Cerfon, F. Sciortino, A. Y. Grosberg, and J. Brujic, Phys. Rev. Lett. **121**, 138002 (2018).
[19] L.-L. Pontani, M. F. Haase, I. Raczkowska, and J. Brujic, Soft Matter **9**, 7150 (2013).
[20] S. Angioletti-Uberti, P. Varilly, B. M. Mognetti, and D. Frenkel, Phys. Rev. Lett. **113**, 128303 (2014).
[21] J. Paredes, M. A. J. Michels, and D. Bonn, Phys. Rev. Lett. **111**, 015701 (2013).
[22] M. A. Jones and C. Ness, Granular Matter **20**, 3 (2018).
[23] D. B. Lukatsky and D. Frenkel, Phys. Rev. Lett. **92**, 068302 (2004).
[24] F. Boyer, É. Guazzelli, and O. Pouliquen, Phys. Rev. Lett. **107**, 188301 (2011).
[25] C. Ness and J. Sun, Phys. Rev. E **91**, 012201 (2015).
[26] K. N. Nordstrom, E. Verneuil, P. E. Arratia, A. Basu, Z. Zhang, A. G. Yodh, J. P. Gollub, and D. J. Durian, Phys. Rev. Lett. **105**, 175701 (2010).
[27] M. van Hecke, J. Phys.: Condens. Matter **22**, 033101 (2009).
[28] I. D. Stoev, Broadband Rheological Characterisation of Soft Functional Materials, Ph.D. thesis, University of Cambridge (2020).
[29] O. Cheal and C. Ness, J. Rheol. **62**, 501 (2018).

[30] J. Israelachvili and D. Tabor, *Progress in Surface and Membrane Science* (Elsevier, Amsterdam, 1973), Vol. 7, pp. 1–55.
[31] S. Plimpton, J. Comput. Phys. **117**, 1 (1995).
[32] C. S. Campbell, J. Fluid Mech. **465**, 261 (2002).
[33] S. Chialvo, J. Sun, and S. Sundaresan, Phys. Rev. E **85**, 021305 (2012).
[34] C. Ness, arXiv:2108.04606 (2021).
[35] J. M. Brader, M. Siebenbürger, M. Ballauff, K. Reinheimer, M. Wilhelm, S. J. Frey, F. Weysser, and M. Fuchs, Phys. Rev. E **82**, 061401 (2010).
[36] K. Hyun, M. Wilhelm, C. O. Klein, K. S. Cho, J. G. Nam, K. H. Ahn, S. J. Lee, R. H. Ewoldt, and G. H. McKinley, Prog. Polym. Sci. **36**, 1697 (2011).
[37] C. Ness, Z. Xing, and E. Eiser, Soft Matter **13**, 3664 (2017).
[38] T. G. Mason, J. Bibette, and D. A. Weitz, Phys. Rev. Lett. **75**, 2051 (1995).
[39] I. M. Krieger and T. J. Dougherty, Trans. Soc. Rheol. **3**, 137 (1959).
[40] E. D. Knowlton, D. J. Pine, and L. Cipelletti, Soft Matter **10**, 6931 (2014).
[41] Y. Otsubo and R. K. Prud'homme, Rheol. Acta **33**, 29 (1994).
[42] T. Mason, Curr. Opin. Colloid Interface Sci. **4**, 231 (1999).
[43] H. A. Barnes, Colloids Surf. A **91**, 89 (1994).
[44] D. Chen, K. W. Desmond, and E. R. Weeks, Soft Matter **8**, 10486 (2012).
[45] C. S. Campbell and C. E. Brennen, J. Fluid Mech. **151**, 167 (1985).
[46] W. M. Jacobs, A. Reinhardt, and D. Frenkel, Proc. Natl. Acad. Sci. USA **112**, 6313 (2015).
[47] C. J. Fullerton and R. L. Jack, J. Chem. Phys. **145**, 244505 (2016).